



LAWRENCE
LIVERMORE
NATIONAL
LABORATORY

Large-scale Gadolinium-doped Water Cerenkov Detector for Non-Proliferation

M. Sweany, A. Bernstein, N. Bowden, S. Dazeley,
R. Svoboda, M. Tripathi

April 11, 2011

Nuclear Instruments and Methods in Physics Research A

Disclaimer

This document was prepared as an account of work sponsored by an agency of the United States government. Neither the United States government nor Lawrence Livermore National Security, LLC, nor any of their employees makes any warranty, expressed or implied, or assumes any legal liability or responsibility for the accuracy, completeness, or usefulness of any information, apparatus, product, or process disclosed, or represents that its use would not infringe privately owned rights. Reference herein to any specific commercial product, process, or service by trade name, trademark, manufacturer, or otherwise does not necessarily constitute or imply its endorsement, recommendation, or favoring by the United States government or Lawrence Livermore National Security, LLC. The views and opinions of authors expressed herein do not necessarily state or reflect those of the United States government or Lawrence Livermore National Security, LLC, and shall not be used for advertising or product endorsement purposes.

Large-scale Gadolinium-doped Water Čerenkov Detector for Non-Proliferation

M. Sweany^{a,b}, A. Bernstein^a, N.S. Bowden^a, S. Dazeley^a, G. Keefer^a, R.
Svoboda^b, M. Tripathi^b

^a*Lawrence Livermore National Laboratory, Livermore, CA 94550, USA*

^b*Department of Physics, University of California, Davis, CA 95616, USA*

Abstract

Fission events from Special Nuclear Material (SNM), such as highly enriched uranium or plutonium, can produce simultaneous emission of multiple neutrons and high energy gamma-rays. The observation of time correlations between any of these particles is a significant indicator of the presence of fissionable material. Cosmogenic processes can also mimic these types of correlated signals. However, if the background is sufficiently low and fully characterized, significant changes in the correlated event rate in the presence of a target of interest constitutes a robust signature of the presence of SNM. Since fission emissions are isotropic, adequate sensitivity to these multiplicities requires a high efficiency detector with a large solid angle with respect to the target. Water Čerenkov detectors are a cost-effective choice when large solid angle coverage is required. In order to characterize the neutron detection performance of large-scale water Čerenkov detectors, we have designed and built a 3.5 kL water Čerenkov-based gamma-ray and neutron detector, and modeled the detector response in Geant4 [1]. We report the position-dependent neutron detection efficiency and energy response of the detector, as well as the basic characteristics of the simulation.

1. Introduction

Legitimate cross border trade involves the transport of an enormous number of cargo containers. In order to verify that these containers are not transporting SNM without impeding legitimate trade, there is a need for fast, highly efficient,

12 and large detectors that are relatively inexpensive. Such detectors must pro-
13 duce consistent yet distinct responses to both SNM and background, so that
14 their effectiveness is not reduced by false positive or negative detections. They
15 also need to have limited sensitivity to background radiation, such as cosmic
16 ray induced background or Naturally Occurring Radioactive Material (NORM)
17 present in certain legitimate forms of cargo. Both of these may contribute to
18 false positives or reduce sensitivity to real SNM.

19 SNM can either spontaneously fission or be induced to do so by an external
20 source of gamma rays or neutrons. Since cargo containers are large, they can
21 contain a significant amount of shielding. The fission emissions most likely to
22 penetrate the container and interact with a detector are neutrons or high en-
23 ergy (greater than 3 MeV) gamma-rays. We propose that a water Čerenkov
24 detector doped with a neutron capturing agent (such as GdCl_3 salt) would be
25 ideal for this application. Such a detector, sensitive to short timescale correla-
26 tions between events, has a number of advantages; it is relatively inexpensive,
27 nonflammable and noncombustible, environmentally safe, and easy to operate.

28 Čerenkov detectors do not produce correlated signals from single fast neu-
29 trons in the same way organic scintillator does: in scintillator, fast neutrons are
30 capable of producing a correlated signal via proton recoil followed by neutron
31 capture. Water Čerenkov detectors only use the thermal neutron capture and
32 prompt gamma-ray signals.

33 Thermal neutron capture on natural Gadolinium has an extremely high cross
34 section (49,000 barns). On capture, a gamma-ray shower with energies adding
35 to approximately 8 MeV is produced, and Čerenkov radiation produced by the
36 resulting Compton scatters is detectable by ordinary PMTs. SNO and Super-
37 Kamiokande have shown that the Čerenkov process can generate enough photons
38 in water to detect neutron captures or gamma-rays with an energy of approxi-
39 mately 3 MeV or greater, so long as the photocathode coverage is high ($\sim 40\%$)
40 [2, 3]. Our group has since demonstrated the viability of this technique above
41 ground, operating 250 liter water based neutron detector with a photocathode
42 coverage of 10%; reflective detector walls made a lower photocathode coverage

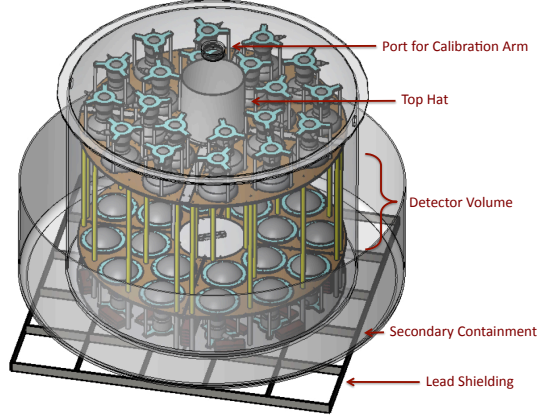


Figure 1: The detector schematic showing the port and top hat for calibration arm insertion. The detector volume is in-between two PMT arrays supported by acrylic rods, and the detector sits inside a secondary containment vessel to protect against accidental leaks. Lead bricks shield against background gamma radiation from the floor.

possible [5].

2. Detector Description

In order to measure the neutron detection efficiency and maximize the performance of a large-scale detector, we have constructed a 3.5 kL water Čerenkov-based neutron detector. The detector consists of a cylindrical polyethylene tank with two PMT arrays arranged on the bottom and top, each with twenty Hamamatsu R7081 10 inch PMTs: although the current generation of R7081 PMTs are high quantum efficiency, the model used here does not have that improvement. The total photocathode coverage is approximately 19%. The tank is approximately 1.5 meter high, with a 2 meter diameter. The detector sits atop a layer of lead bricks to shield against background gamma radiation from the floor. Figure 1 shows a schematic of the detector: the white cylindrical opening in the center, called the top hat, allows for deployment of calibration sources

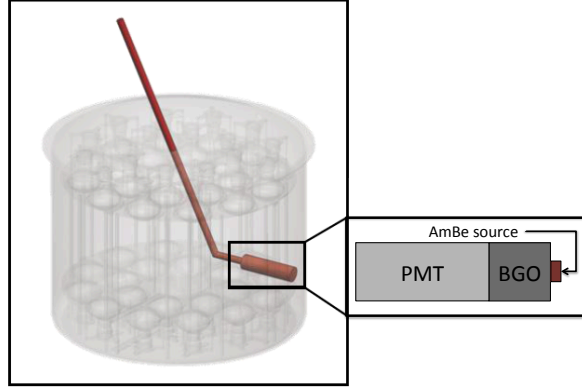


Figure 2: The neutron calibration arm: the PMT reads out gamma radiation coming from the AmBe source.

at several locations inside the detector through a 10 cm diameter portal in the lid. The calibration source sits at the end of a long arm (the calibration arm), shown in Figure 2 and discussed further below.

It has been demonstrated that GdCl_3 doped water is not compatible with stainless steel, contact with which results in reduced water clarity [4]. All detector components in contact with the water are therefore constructed of either plastic or glass. The PMTs are mounted on a frame constructed out of acrylic and white polypropylene that sits inside the tank, shown in Figure 3a. Each detector quadrant contains ten PMTs, five each on the top and bottom, with the top PMT array supported by acrylic rods. Because the frame structure and PMTs are buoyant, stainless steel bars (sealed inside polypropylene bags) are used as ballast. Figure 3b, shows the bottom four quadrants with the support rods in place. To increase light collection, the detector wall in between the two PMT arrays is lined with UV reflecting Teflon.

The detector is filled from the bottom using a water purification system capable of obtaining ultra pure deionized water (resistivity greater than $17 \text{ M}\Omega\cdot\text{cm}$).

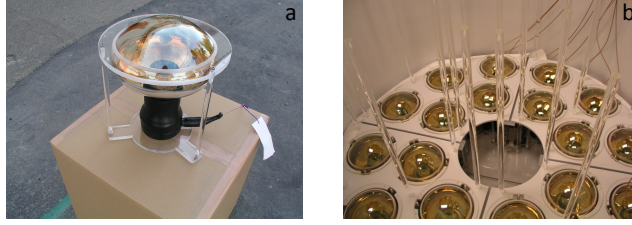


Figure 3: A Hamamatsu R7081 PMT with factory water proof potting (a), and the bottom 20 PMTs installed in the bottom detector array (b).

72 Municipal water is passed through three large de-ionizing (DI) resin bottles and
 73 is then circulated through a purification system purchased from South Coast
 74 Water Inc., consisting of a UV sterilizer, 5 micron and 0.22 micron filters, and
 75 an additional DI unit. Each unit in the system can be by-passed through a series
 76 of valves. After purification, the DI unit is by-passed and the water is doped
 77 with GdCl_3 . Any particulate matter and remaining biological contamination
 78 from the GdCl_3 is eliminated by continued re-circulation through the filters and
 79 UV sterilizer. Finally, the doped water is sent to the detector inlet.

80 2.1. Data Acquisition

81 The DAQ and trigger electronics are mostly commercial VME and NIM
 82 modules. The only modules designed and fabricated in-house are eight-channel
 83 signal pick-off modules. The pick-off modules are needed to separate the fast
 84 PMT signal from the high voltage bias, which is carried on the same cable
 85 coming out of the PMT.

86 From there, the PMT signals are passed through a Mini-Circuits 15542
 87 BB LP-39+, 23 MHz low-pass filter in order to stretch out the signal, then am-
 88 plified and digitized using CAEN V975 amplifiers and 200 MHz Struck SIS3320
 89 digitizers. There are two triggers for the system: an internally generated trigger
 90 for physics events in the water and an external trigger used for calibration. The
 91 internal trigger is formed from a four-fold coincidence among a group of 16 bot-
 92 tom PMT channels. The PMT signals are fed to a CAEN V814 discriminator,

93 set to trigger at ~ 1 photo-electron. A CAEN V1495 FPGA registers the 4-fold
94 coincidences and issues the trigger to the waveform digitizers.

95 **3. Calibration and Detection Efficiency**

96 Calibration of the detector is needed to equalize the PMT gains and to set
97 an approximate energy scale for physics events. We have three artificial sources:
98 an LED for PMT gain, a ^{252}Cf fission source for neutrons, and a tagged neutron
99 source to measure the neutron detection performance on an event-by-event basis.
100 A polyethylene calibration arm was constructed in collaboration with a group
101 at Harvey Mudd College to deploy the neutron sources at multiple positions
102 inside the detector.

103 The tagged neutron source consists of an americium beryllium (AmBe)
104 source and a Scionix type 51B51/2M-E1-BGO crystal and PMT deployed to-
105 gether inside the calibration arm. AmBe sources emit a neutron in coincidence
106 with a 4.4 MeV gamma-ray. Detection of this gamma-ray by the BGO detector
107 forms a "tag", indicating that a neutron has been emitted from the source. A
108 rendering of the crystal, PMT, and AmBe source inside the polyethylene arm
109 is shown in Figure 2. The arm was designed so that it can reach several posi-
110 tions inside the detector, making position dependent neutron detection efficiency
111 measurements possible.

112 *3.1. ^{252}Cf Calibration*

113 Three datasets were taken with a ^{252}Cf source positioned at various locations
114 outside the detector: seven inches from the detector wall, one meter from the
115 detector wall, and two meters from the detector wall. The first position is used
116 to calibrate the response from Monte Carlo and to establish the quality of event-
117 level cuts on the data. The one and two meter positions are used to determine
118 how the event-level cuts perform with distant sources.

119 Since high energy events, such as muons traversing the detector tend to
120 saturate the response of the PMTs, we first screen our data to remove all events

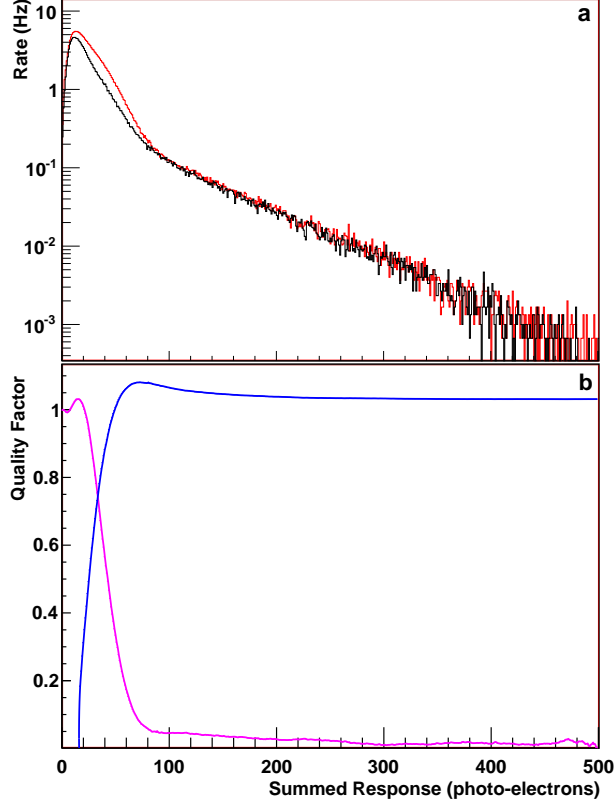


Figure 4: In (a), the correlated (red) and uncorrelated (black) summed response with the ^{252}Cf source seven inches from the detector edge: the high-energy tail is due to cosmic-ray induced muons and gamma-rays. The charge quality factor for left (pink) and right (blue) cuts is shown in (b), where the maximum in the quality factor is used to establish the cut values.

121 that contain at least one saturated PMT. Event level cuts are then applied to
 122 select neutrons in the detector. Each is determined by maximizing a Quality
 123 Factor, Q , defined as the significance after the cut is applied divided by the
 124 significance before the cut is applied. For a given parameter distribution divided
 125 into n independent bins, and for an analysis cut at the j th bin, the quality factor
 126 approaching from the left, or lower bound, is

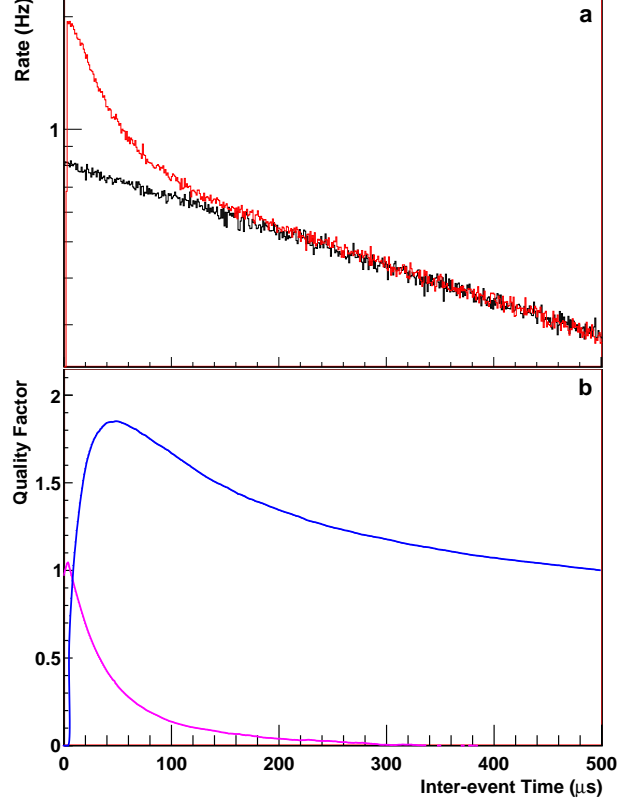


Figure 5: In (a), the inter-event time for events passing the charge cut (red), and the fit to the uncorrelated background (black). The time quality factor for left (pink) and right (blue) cuts is shown in (b), where the maximum in the quality factor is used to establish the cut values.

$$Q_j^L = \left(\frac{\sum_{i=0}^j \text{On}_i - \sum_{i=0}^j \text{Off}_i}{\sqrt{\sum_{i=0}^j \text{Off}_i}} \right) \left(\frac{\sqrt{\sum_{i=0}^n \text{Off}_i}}{\sum_{i=0}^n \text{On}_i - \sum_{i=0}^n \text{Off}_i} \right),$$

127 where On and Off represent the value of the parameter with and without
128 the neutron source present, respectively. Q is defined to have a value equal to 1
129 when no cut is applied, i.e. when j equals n . Once a lower bound cut value has

130 been determined, we then apply the same formula in reverse, or from the right,
 131 to determine the best j th bin for an upper bound cut:

$$Q_j^R = \left(\frac{\sum_{i=n}^j \text{On}_i - \sum_{i=n}^j \text{Off}_i}{\sqrt{\sum_{i=n}^j \text{Off}_i}} \right) \left(\frac{\sqrt{\sum_{i=0}^n \text{Off}_i}}{\sum_{i=0}^n \text{On}_i - \sum_{i=0}^n \text{Off}_i} \right).$$

132 The quality analysis for charge is shown in Figure 4. Because the fission
 133 source increases the number of uncorrelated gamma-rays interacting in the de-
 134 tector, using the on source uncorrelated background as the no source present
 135 histogram for the quality analysis provides better rejection of gamma energies.
 136 In Figure 4a, the correlated on source data is shown in red and the uncorrelated
 137 on source is shown in black. Figure 4b shows Q for the left (pink) and right
 138 (blue) cuts. The resulting cuts are applied to both the current event and the
 139 previous event to establish neutron-neutron pair events in the detector.

140 Since the presence of a neutron source results in an increase in the uncor-
 141 related trigger rate, a comparison of the inter-event time distribution with and
 142 without the source is not appropriate. Instead, the random trigger rate in the
 143 on source data is fit to an exponential, and a histogram filled randomly from
 144 the fit values serves as the no source present histogram. The results shown in
 145 Figure 5 with the on source inter-event time, as well as the quality factor.

146 In order to pick out neutron-neutron events, we cut on both the current
 147 event and the previous event charge. Finally, we reject events in which the
 148 time difference between the current event and the last muon is less than 46
 149 μs , which acts as a muon veto; the value is chosen as the same maximum inter-
 150 event time value allowed. A muon veto cut of 46 μs rejects 9.9% of the correlated
 151 background and increases the dead-time of the detector by 2.5%. Although there
 152 is modest improvement in rejecting muon-induced backgrounds, the majority of
 153 cosmic backgrounds appear to result from muons in the vicinity of the detector
 154 but not traversing it. The final cut values for all four event-level cuts are shown
 155 in Table 1.

156 Table 2 shows the event rates averaged over 20 seconds for the data run with

Parameter	Left Cut	Right Cut
Current Charge	16 pe	72 pe
Previous Charge	16 pe	72 pe
Inter-event Time	4 μ s	46 μ s
Muon Veto	>46 μ s	N/A

Table 1: Analysis cuts obtained by maximizing the signal significance between the background data run and ^{252}Cf data run with the source seven inches from the detector.

Event Rate (Hz)	^{252}Cf Source	No Source
Raw	2390	1770
Singles	920	468
Doubles	55.0	13.7

Table 2: Average event rates over 20 seconds for ^{252}Cf data run with the source seven inches from the detector, compared with no source present. The singles rate has only the energy cut and a muon veto applied, and the doubles rate has all cuts applied.

the ^{252}Cf source seven inches from the detector edge compared to no source present. At this position, the solid angle coverage is 28% of 4π . The singles rate, or the rate of single neutron events in the detector, is the rate after both an energy cut on the current event and the muon veto cut has been applied. The doubles rate, or the rate of neutron-neutron pair events, is the rate after all cuts in Table 1 have been applied.

3.2. Neutron Detection Efficiency

The neutron detection efficiency is determined using the calibration arm described above. The AmBe gamma-ray spectrum from the BGO crystal in Figure 6 shows the primary 4.4 MeV gamma-ray peak. The smaller peaks at 3.9 MeV and 3.4 MeV are also due to 4.4 MeV gamma-rays, where pair production and subsequent positron annihilation results in either one or two 511 keV gamma-rays escaping from the crystal. To maximize the signal to background ratio of our tag, we select events in the range 3 MeV to 5 MeV, where the background gamma-ray rate in the crystal is very small. Figure 7

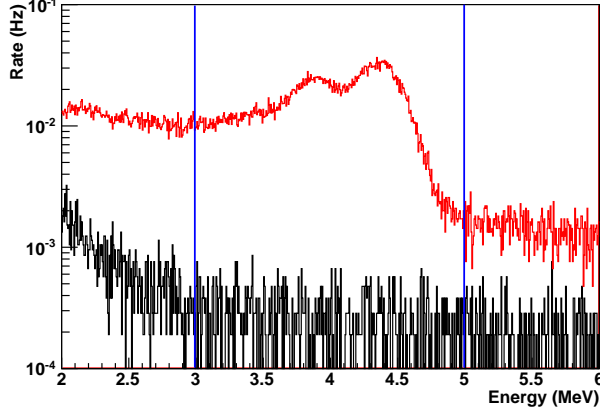


Figure 6: The charge from the BGO crystal with (red) and without (black) an AmBe source present. The energy cuts around the 4.4 MeV gammas and two escape peaks are shown in blue.

172 shows the timing distribution of delayed detector events after our selection of
 173 AmBe tags. This inter-event time distribution can be well parameterized by
 174 a sum of two exponentials, representing a correlated and uncorrelated set of
 175 events. The correlated set represents neutron capture events due to the AmBe
 176 source in our detector. The mean capture time is $35 \mu\text{s}$. This is consistent
 177 with the expected capture time of thermal neutrons in water doped with 0.1%
 178 gadolinium [5–8]. The number of neutron captures detected can be estimated
 179 by subtracting the exponential fit to the un-correlated events. The efficiency is
 180 taken to be the integral of the correlated events, the black curve in Figure 7,
 181 divided by the total number of neutron tags (after accounting for the crystal's
 182 background rate), or the red curve in Figure 7.

183 Three AmBe data sets were taken inside the detector to determine the ef-
 184 ficiency and energy response at various radii. We assume that the detector is
 185 radially symmetric. One dataset was taken outside the detector, for which the
 186 efficiency is multiplied by the fraction of solid angle calculated from the source
 187 position. The position-dependent efficiency is shown in Figure 8; it ranges from
 188 69.9% at the center of the detector to 31.3% outside the detector. The efficiency

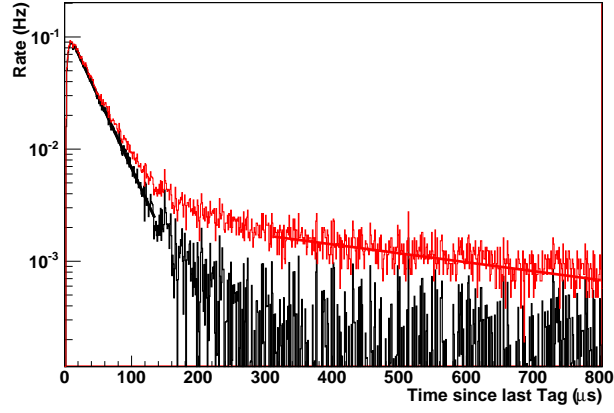


Figure 7: The time between tag and detector triggers for all events (red). In the 300-800 μs range are the uncorrelated accidentals. The correlated events in the 0-100 μs range, with the uncorrelated background subtracted (black), indicate a capture time of 35 μs .

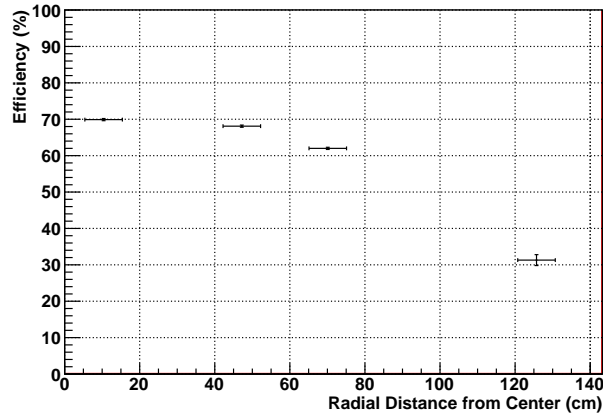


Figure 8: The neutron detection efficiency verses the AmBe source position. For the position outside the detector (125 cm), the efficiency has been scaled by the solid angle coverage of the detector.

189 drop is expected near the detector edge, as neutrons can leave before being cap-
 190 tured and many of the neutron capture gamma-rays escape the detector before
 191 interacting.

192 3.3. Monte Carlo Response

193 A full Monte Carlo was written in Geant4 to model our detector. Our
194 objective is to utilize the Monte Carlo, tuned to reproduce the response of this
195 detector, to determine the best design for a larger-scale detector.

196 The output of the Monte Carlo is the wavelength of photon hits on the PMT
197 surfaces. In analysis, an energy-dependent quantum efficiency is applied, and a
198 variable single photo-electron response is applied to each photo-electron. The
199 trigger is modeled by requiring at least four PMT signals to be greater than a
200 given threshold. The detector data is then scaled by the PE to ADC unit value
201 determined from single photo-electron calibrations.

202 There are three optical properties that can be tuned to reproduce the re-
203 sponse in data: the wall reflectivity, the attenuation length of water, and, to a
204 limited extent, the PMT quantum efficiency. The attenuation length of water in
205 our detector was likely adversely affected by UV stabilizers in the polyethylene
206 tank. The attenuation length from [9–11] scaled down to an approximately 10
207 meter maximum gave results consistent with our data. The quantum efficiency
208 is taken from Hamamatsu specifications, and scaled down to account for losses
209 in collection efficiency from stray magnetic fields: the total efficiency peaks at
210 22%. Finally, the wall reflectivity has a total reflectivity of 90% with a 5%
211 specular component.

212 Good agreement between data and Monte Carlo has been obtained with
213 both AmBe source data inside the detector (Figure 9) and the ^{252}Cf source data
214 outside the detector (Figure 10). For the AmBe comparison, the calibration arm
215 is included in the Monte Carlo.

216 4. Discussion and Conclusions

217 Based on the average number of neutrons produced from our ^{252}Cf source,
218 as well as the average number of neutrons produced in reactor grade plutonium
219 (RGP), we have determined that our current setup can detect approximately

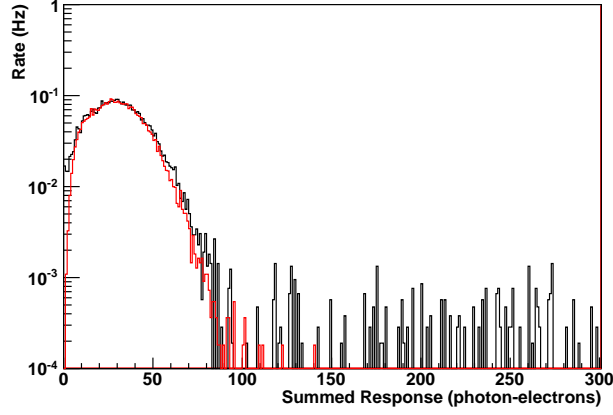


Figure 9: The pure neutron spectrum obtained from the tagged-calibration arm positioned inside the detector (black) compared with the MC spectrum from 5 MeV neutrons generated at the center of the detector (red).

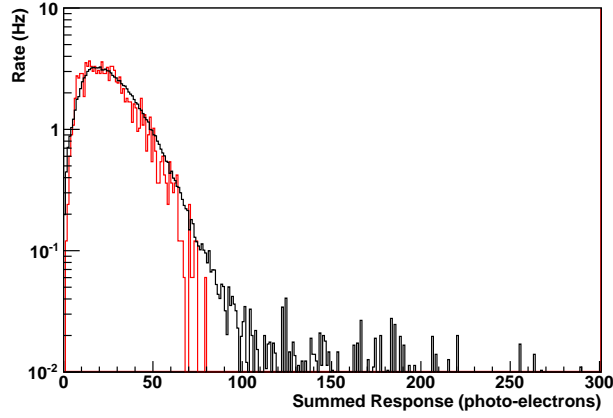


Figure 10: The pure neutron spectrum obtained from a ^{252}Cf source positioned 7 inches from the detector edge (black) compared with the MC spectrum from 5 MeV neutrons, 7 inches from the detector edge.

220 150 g equivalent of RGP over background at two meter standoff from the detec-
 221 tor edge in 20 seconds. The solid angle presented by our detector at this distance
 222 is 2.4% of 4π . We have assumed 8% fraction of ^{240}Pu in RGP (87,000 n/s/kg).
 223 Figure 11 is the signal over background for each cut in Table 1 as a function

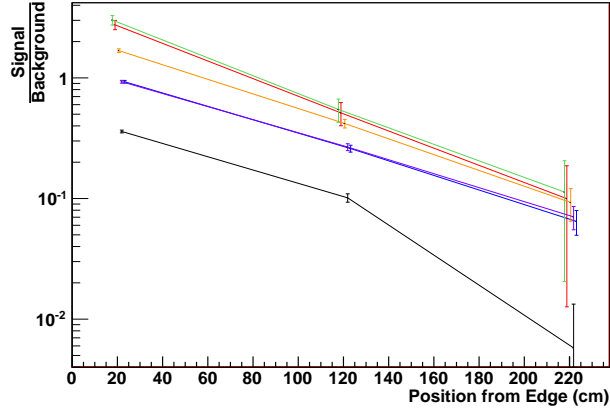


Figure 11: The signal-over-background ratio for ^{252}Cf adjacent to the detector, one meter from the detector's edge, and two meters from the detector edge. The colors correspond to no cuts (black), the charge cut on the current event (blue), the current charge and muon veto cut (purple), the charge cut on the current and previous event (orange) resulting in neutron-neutron pairs, the neutron-neutron pairs plus the timing cut (red), and the neutron-neutron pairs plus the timing cut with the muon veto (green). There is an arbitrary offset in the x-axis as a visual aid: the green curve corresponds to the true radial position.

of radial distance from the detector. At one meter from the detector edge, or 6.4% of 4π , we have a signal to background ratio of 0.547 ± 0.120 after all cuts have been made. Before cuts, the signal over background was 0.101 ± 0.00810 . At two meters, the signal over background before cuts is 0.00560 ± 0.00755 and increases to 0.113 ± 0.0927 after all cuts have been made. Since our detector is intended as a correlated event detector, it is expected that high solid angle coverage is required for efficient operation. However, with the proper event-level cuts our source is detectable even at two meters away: without requiring neutron-neutron pairs, the signal over background is 0.0702 ± 0.0154 .

4.1. Next Generation Detector

There are many ways to improve the performance of this detection technology. Aside from optical and geometrical optimizations, decreasing the neutron capture window by increasing the concentration of GdCl_3 will result in a de-

crease in the rate of accidental coincidences. An examination of this detector's ^{252}Cf calibration data shows that if the neutron capture window was decreased from $35\ \mu\text{s}$ to $10\ \mu\text{s}$, and assuming the same number of neutrons are captured, the percentage of accidental coincidences drops from 53% of all events surviving the current and last event energy cuts to 23%. In other words, if all neutrons are captured within $10\ \mu\text{s}$, then for every 4.3 coincident events, one would be accidental. This is a significant improvement compared to our current concentration in which all neutrons are captured within $35\ \mu\text{s}$: for every 1.9 coincident events, one is accidental. It has been shown that there is no measurable impact on water attenuation length at the level of 0.2% GdCl_3 [4]. An increase in GdCl_3 concentration to the 0.3% level is needed to obtain a characteristic capture time of $\sim 10\ \mu\text{s}$. Further study may be warranted in this area.

4.2. Conclusions

We have successfully operated a large-scale gadolinium-doped water Čerenkov detector and characterized its neutron detection performance for the purposes of SNM monitoring. Using a tagged americium beryllium source, the raw neutron detection efficiency has been measured in the center of the detector at 70% and outside the detector at 31%. Event-level cuts have been established to maximize the detection of correlated pairs of neutrons emitted simultaneously from a ^{252}Cf fission source. We have demonstrated detection of approximately 150 g equivalent of RGP over background within 20 seconds for a solid angle coverage of 2.4% of 4π ; an optimized geometry is expected to perform even better.

The neutron capture response of the detector has been reproduced in Geant4 for two different source positions, using the water attenuation length, the PMT quantum efficiency, and the wall reflectivity as tuning parameters. The tuned value of each parameter is within the expected range for the water quality, PMTs, and Tyvek reflectivity. Future work will use this model to design an optimized radiation portal monitoring system for detection of correlated neutrons from undeclared fission sources within cargo containers.

266 Acknowledgements

267 The authors would like to thank Dennis Carr for assistance with detector
268 design and construction, as well as Serge Ouedraogo for help with construction.
269 The authors also wish to thank the DOE NA-22 for their support of this project.

270 This work was performed under the auspices of the U.S. Department of
271 Energy by Lawrence Livermore National Laboratory under Contract DE-AC52-
272 07NA27344. Document release number LLNL-JRNL-479935.

273 References

- 274 [1] J. Allison *et. al.* “Geant4 developments and applications” *IEEE Transactions*
275 *on Nuclear Science* **53(1)** (2006) p. 270.
- 276 [2] The SNO Collaboration. “Electron energy spectra, fluxes, and day-night
277 asymmetries of ^8B solar neutrinos from measurements with NaCl dissolved
278 in the heavy-water detector at the Sudbury Neutrino Observatory” *Physical*
279 *Review C* **72** (2005) 055502.
- 280 [3] The Super-Kamiokande Collaboration. “Solar neutrino measurements in
281 Super-Kamiokande-I” *Physical Review D* **73** (2006) 112001.
- 282 [4] W. Coleman, A. Bernstein, S. Dazeley and R. Svoboda. “Transparency of
283 0.2% GdCl₃ doped water in a stainless steel test environment” *Nuclear*
284 *Instruments and Methods A* **595** (2008) p. 339.
- 285 [5] S. Dazeley, A. Bernstein, N.S. Bowden, and R. Svoboda. “Observation of
286 neutrons with a Gadolinium doped water Cherenkov detector” *Nuclear In-*
287 *struments and Methods A* **607** (2009) p. 616.
- 288 [6] M. Apollonio *et. al.* “Search for neutrino oscillations on a long base-line at
289 the CHOOZ nuclear power station” *European Physical Journal C* **27** (2003)
290 p. 331.
- 291 [7] F. Boehm *et. al.* “Final results from the Palo Verde neutrino oscillation
292 experiment” *Physical Review D* **64** (2001) 112001.

- 293 [8] A. B. Piepke, S.W. Moser, and V.M. Novikov. “Development of a Gd loaded
294 liquid scintillator for electron anti-neutrino spectroscopy” *Nuclear Instru-*
295 *ments and Methods A* **432** (1999) p. 392.
- 296 [9] T. I. Quickenden and J. A. Irvin. “The ultraviolet absorption spectrum of
297 liquid water” *Journal of Chemical Physics* **72 (8)** (1980) p. 4416.
- 298 [10] F. M. Sogandares and E. S. Fry. “Absorption spectrum (340 - 640 nm)
299 of pure water. I. Photothermal measurements” *Applied Optics* **36** (1997) p.
300 8699.
- 301 [11] R. M. Pope and E. S. Fry. “Absorption spectrum (380 - 700 nm) of pure
302 water. II. Integrating cavity measurements” *Applied Optics* **36** (1997) p.
303 8710.